THE JOURNAL OF PHYSICAL CHEMISTRY C

Article

Ab Initio Atomistic Thermodynamics Study of the (001) Surface of LiCoO in a Water Environment and Implications for Reactivity under Ambient Conditions

Xu Huang, Joseph William Bennett, Mimi N. Hang, Elizabeth D. Laudadio, Robert J Hamers, and Sara E. Mason

J. Phys. Chem. C, **Just Accepted Manuscript** • DOI: 10.1021/acs.jpcc.6b12163 • Publication Date (Web): 07 Feb 2017

ACS Publications

The Journal of Physical Chemistry C is published by the American Chemical Society. 1155 Sixteenth Street N.W., Washington, DC 20036

Ab Initio Atomistic Thermodynamics Study of the (001) Surface of $LiCoO_2$ in a Water Environment and Implications for Reactivity under Ambient Conditions

Xu Huang [1], Joseph W. Bennett [1], Mimi N. Hang [2], Elizabeth D. Laudadio [2], Robert J. Hamers [2] and Sara E. Mason [1]**

1: Department of Chemistry

University of Iowa, Iowa City, Iowa 52242;

2: Department of Chemistry

University of Wisconsin-Madison, Madison, WI 53706

E-mail: sara-mason@uiowa.edu

Abstract

We use GGA + U methodology to model the bulk and surface structure of varying stoichiometries of the (001) surface of $LiCoO_2$. The DFT energies obtained for these surface-slab models are used for two thermodynamic analyses to assess the relative stabilities of different surface configurations, including hydroxylation. In the first approach, surface free energies are calculated within a thermodynamic framework, and the second approach is a surface-solvent ion exchange model. We find that for both models, the -CoO-$H_{1/2}$ surface is the most stable structure near the O-rich limit, which corresponds to ambient conditions. We find that surfaces terminated with Li are higher in energy, and we go on to show that H and Li behave differently on the (001) $LiCoO_2$

surface. The optimized geometries show that terminal Li and H occupy nonequivalent surface sites. In terms of electronic structure, Li and H terminations exhibit distinct bandgap character, and there is also a distinctive distribution of charge at the surface. We go on to probe how the variable Li and H terminations affect reactivity, as probed through phosphate adsorption studies.

Introduction

One of the grand challenges of modern science and engineering is to develop sustainable technologies to address fundamental societal needs such as improved human health,[1] cleaner means of producing and storing energy,[2] and reducing the negative environmental impact posed by large-scale manufacturing across a variety of industries.[3,4] The most prominent effort in technological development over the last fifteen years has been the manufacturing and deployment of nanomaterials for everyday use. We encounter nanomaterials everyday; they serve as resistant surface coatings, additives to textiles and cosmetics, and compose most modern construction materials.[5] Progress here has advanced rapidly due to major scientific breakthroughs related to the fundamental understanding of functional properties related to, synthesis of, and subsequent use of a variety of nanomaterials.

Two fields in which nanomaterials are finding widespread use are medicine and energy storage. Gold nanoparticles are actively being investigated as reactive probes, components of improved imaging agents, and as the vehicle for targeted drug delivery.[6,7] Silicon nanowires,[8] silicon nanotubes,[9] and Si-embedded graphite[10] are finding use in battery applications, most likely due to the versatile nature of synthetically controllable nanostructure shapes and motifs. These different structural motifs demonstrate tunable physical properties unique to the nanomaterial, such as nano-networks to enhance electronic conduction[11] or tailorable core-shell structures to promote thermoelectric effects,[12] making it advantageous to use nanomaterials in an increasing variety of new ways.

This increase in use of nanomaterials has also led to the release of a substantial amount of nanoparticles into the environment, where the effects of these materials are most times unknown, especially at the nano-bio interface.[13–15] Recent studies would indicate that the properties of nanoparticles are sometimes detrimental: transition metal oxides can participate in oxidation reduction reactions that create reactive oxygen species that damage cellular components, and unfavorable chemical transformations such as dissolution and aggregation can occur that are dependent upon chemical environment.[16,17] This is especially noticeable for nanomaterial surfaces that are just beginning to be probed; recent examples include studies on silica,[18] titania,[19] gold[20,21] and Li-intercalated transition metal oxides.[22,23]

$LiCoO_2$ (LCO) is a transition metal oxide that functions as one of the primary cathode components of mass-produced Li-ion batteries.[24,25] The use of this oxide as a nanomaterial has witnessed rapid growth in commercial and industrial applications[26–31] as LCO (and related) nanoparticles yield enhanced lithium transport, better electrical conduction, and reduced fragmentation from mechanical stresses exhibited during lithium (de)intercalation.[23,27,32–36] Some of the rapid growth in these applications can be attributed to computational efforts designed to understand and optimize the complex nature of LCO, its properties, and related battery materials,[37–55] which has led to almost revolutionary advancement in the interplay of theoretical modeling and experimental techniques.[56]

To strengthen this interplay, we can use computational methods to develop models that go beyond the thermodynamic ground state to elucidate processes linked to experimentally quantifiable metrics, such as surface mediated reactivity. In this manner, we can correlate the changes in surface structure over a wide range of chemical environments to the surface mediated processes that result because of those changes. Differences in environmental conditions will transform the surface structure, and that change in the surface structure will affect the reactivity of the surface, as well as any surface mediated pathways related to the adsorption or release of ions, and ultimately toxicity. A recent example of the need for the development of this type of model is the observation of a negative biological impact on Shewanella oneidensis MR-1 caused by the release of transition metal cations from Li-ion battery materials[23] in aqueous solution. Since Li-ion batteries encounter only aprotic organic solvents, their preferred surface structures and reactivity in polar solvents such as water is as of yet mostly unexplored. If these materials are being mass-produced and (if not properly recycled) find their way into a hydrous environment, then we need to understand how they will behave at the nano-bio interface.

What has also received little attention in the field of surface mediated processes is the adsorption of small, biologically relevant ions under ambient conditions, and how these environmentally acquired coatings might act as protective layers. We choose phosphate as our probe adsorbate, as it is a key nutrient to a variety of organisms, and phosphorous is a key component of industrial battery material coating. At environmentally relevant pHs and concentrations, if phosphate binds irreversibly to metal oxide cathode materials, this could have ecobiological implications if the material is released into the environment. Beyond biological concerns, phosphate adsorption on metal oxides is critical to investigate since industrial LCO surface coatings incorporate phosphorous as the amorphous LiPON,[57] or as an ordered metal phosphate such as AlPO4.[58] It has been demonstrated that the functional properties and chemical behavior of LCO nanoparticles improves with these surface adsorbed coating layers, as the coating can enhance directed ionic transfer, act as a scavenger for HF released from solid state electrolytes, and act as a chemically stable barrier to protect the LCO surface from attack in aqueous environments.[59–65]

What has not yet been demonstrated is the mechanism of interaction and bonding at the interface of these coatings with the LCO surface, specifically in an atomistic framework. Moreover, there is a dearth of understanding how LCO itself will respond in an aqueous environment, as most surface studies of this material are performed under vacuum or other carefully tuned laboratory conditions.[66,67] Experimental XRD measurements on LCO nanoparticles have confirmed the existence of various $LiCoO_2$ nanoparticle surface directions, such as (001), (104) and (110),[68,69] and it has also been demonstrated that the H_2O molecule has a low adsorption energy on those facets.[70] These two facts warrant investigation into the hydrated surface structure and reactivity of $LiCoO_2$ in an ambient environment, beyond the purely biological impact of the nanomaterial.

In this manuscript, we report the results of a GGA+U study that uses two thermodynamic modeling approaches to predict the surface structure of the LCO (001) surface exposed to water. The surface studies suggest that Li and/or OH coverage persists over a wide range of modeled conditions. However, terminal Li and H are found to occupy distinct surface sites, and also give rise to disparate charge density distributions at the surface. The implications of Li or OH terminations on reactivity are probed through model adsorption with phosphate ions, which also provides fundamental insight into the mechanisms that govern both the environmental and industrial coating of battery materials.

Methodology

Periodic DFT calculations[71,72] of bulk and surface $LiCoO_2$ are performed using the PBE-GGA exchange-correlation functional[73] in the open source Quantum-ESPRESSO software package.[74] All atoms are represented with ultrasoft pseudopotentials,[75] and all calculations have a plane-wave cutoff of 40 Ry for the wavefunction and 320 Ry for the charge density. All atoms were allowed to fully relax during structural optimizations, and the convergence criteria for the self-consistent relaxation was a maximum residual force of 10^{-2} eV $\cdot$Å^{-1} per atom. An 8×8×8 Monkhorst–Pack k-point mesh[76] was used in hexagonal bulk $LiCoO_2$ calculations. For the $LiCoO_2$ (001) surface simulations, the slabs are constructed such that two equivalent, symmetry-related surfaces are exposed, and the energy is sampled using k-point meshes of 8×8×1 and 4×4×1 in (1×1) and (2×2) surface supercells, respectively. Each surface relaxation has at least 16 Å of vacuum to prevent the surface from interacting with its own periodic repeats.

As Co is a 3d-transition metal, we apply a Hubbard U correction to account for the over-delocalization observed in DFT-methods.[77–80] We employ a $U^d = 4.91$ eV, previously derived from first-principles linear response theory[81] for layered Co^{3+} oxides.[33]

All of the Quantum-Espresso calculations are carried out with the surface slab exposed to vacuum. In order to model phosphate adsorption under aqueous conditions, additional calculations were carried out using the $DMol^3$ code developed by Delley,[82,83] applying a continuum solvation model.[84] Further details of the $DMol^3$ calculations are provided in the Supporting Information (SI).

Surface Free Energy Thermodynamics

The stabilities of varying surface stoichiometries in vacuum are compared in terms of the surface free energy, γ, using the first-principles thermodynamics framework developed by Reuter and co-workers,[85–87] and as previously applied to the $LiCoO_2$ system[34] Here, we review key aspects of the method as it pertains to the LCO systems under study here, as the details of the full method have been presented in the works by Reuter and co-workers. At specific conditions of T and p we choose one atomic species (Co in this work) to have an equivalent chemical potential, μ_i, in all the phases present in the entire system. This means that the surface free energy, $\gamma(T,p)$, can be written as the difference between the Gibbs free energy of the surface slab (G_{slab}) and the sum of all the chemical potentials multiplied by their corresponding atom count (N_i), and divided by twice the surface area (A):

$$\gamma(T,p,N_i) = \frac{1}{2A}\{G^{\mathrm{slab}}(T,p,N_i) - \sum_i N_i\mu_i(T,p)\} \quad (1)$$

$$= \frac{1}{2A}\{G^{\mathrm{slab}}_{\mathrm{LiCoO_2}}(T,p,N_i) - N_{\mathrm{Li}}\mu_{\mathrm{Li}} - N_{\mathrm{Co}}\mu_{\mathrm{Co}} - N_{\mathrm{O}}\mu_{\mathrm{O}} - N_{\mathrm{H}}\mu_{\mathrm{H}}\} \quad (2)$$

where the factor of $2A^{-1}$ normalizes $\gamma(T,p,N_i)$ the surface free energy per unit area for a slab of two surfaces with inversion symmetry. The range of μ_{O} at 0 K is defined by the oxygen-rich and -poor extremes at the phase transition limits on the surface. Using the fact that the DFT total energy can be directly related to the Gibbs free energy at 0 K, and considering the oxygen-rich limit as occurring when gas-phase oxygen condenses at the surface, it can be written that:

$$\mu_{\mathrm{O,max}} = \frac{1}{2} E_{\mathrm{O_2}} \tag{3}$$

where $E_{\mathrm{O_2}}$ is the total energy of one O_2 gas molecule calculated by DFT. At the oxygen-poor limit, the $LiCoO_2$ surface decomposes into bulk metal cobalt and lithium, and gas-phase O_2. We define the oxygen-poor limit based on the equilibrium of $LiCoO_2 = Li + Co + O_2$:

$$\mu_{\mathrm{O,min}} = \frac{1}{2} [E_{\mathrm{LiCoO_2,bulk}} - E_{\mathrm{Co,bulk}} - E_{\mathrm{Li,bulk}}] \tag{4}$$

where $E_{\mathrm{LiCoO_2}}$ is the total energy of a single $LiCoO_2$ unit. In previous theoretical studies using this thermodynamic approach, the oxides studied contain only one metal species,[88–90] and the other chemical potentials can all be related to μ_{O}. In the case of $LiCoO_2$ where there are two metal species, one of them becomes an additional variable in the phase diagram. Here we chose Li as the second dimension of the phase diagram in the same method in Kramer's work.[34] In this approach, the Li-rich and -poor limits can be written as:

$$\mu_{\mathrm{Li,max}} = E_{\mathrm{Li,bulk}} \tag{5}$$

$$\mu_{\mathrm{Li,min}} = E_{\mathrm{LiCoO_2,bulk}} - E_{\mathrm{Co,bulk}} - E_{\mathrm{O_2}} \tag{6}$$

The chemical potential of hydrogen (μ_{H}) at 0 K can be determined using an equilibrium with μ_{O} and either a H_2 molecule or H_2O.[90] Here we apply the second equilibrium as:

$$\mu_{\mathrm{H}} = \frac{1}{2}(E_{\mathrm{H_2O,gas}} - \mu_{\mathrm{O}}) \tag{7}$$

Therefore Equation 2 can be re-written as:

$$\gamma(T,p,N_i) = \frac{1}{2A}[G^{\mathrm{slab}}_{\mathrm{LiCoO_2}} - N_{\mathrm{Co}}\mu^{\mathrm{bulk}}_{\mathrm{LiCoO_2}} + (N_{\mathrm{Co}} - N_{\mathrm{Li}})\mu_{\mathrm{Li}} + (2N_{\mathrm{Co}} - N_{\mathrm{O}} + \frac{1}{2}N_{\mathrm{H}})\mu_{\mathrm{O}} - \frac{1}{2}N_{\mathrm{H}}E_{\mathrm{H_2O,gas}}] \tag{8}$$

where $\mu_{\mathrm{O,max}}$ and $\mu_{\mathrm{Li,max}}$ are re-scaled to zero along the μ_{O} and μ_{Li} axes in the phase diagram, respectively, while the calculated γ can be solved for explicitly for each surface in vacuum.

The surface free energy calculations are extended to finite (T,p) conditions that take into account the distinct molecular, bulk, and slab contributions to the free energy. This methods are described in detail in the works of Reuter and co-workers. Experimentally relevant O_2 partial pressure ranges are 10^2-10^{-12} Torr. This corresponds to the range observed from ambient conditions down to ultra-high vacuum chambers. This range is represented theoretically as a shift in the 0 K value of μ_O of $\approx$0.7 eV. The influence of these finite pressure conditions are presented and discussed in the context of the calculated surface phase diagrams presented in this study.

In terms of the surface slabs, high-frequency phonon modes may contribute an additional term to the surface free energy in a non-uniform way as a function of surface stoichiometry. We use the definition of vibrational temperature, $\theta_{\nu_i}=h\nu_i/k_{\mathrm{B}}$, to obtain the zero point energy of high-frequency OH modes on the surface of our hydrated oxides. We obtain a total contribution of 0.217 eV per OH which is then multiplied by the total number of OH groups on the surface, following the procedure of Sun *et al.*[86] These calculations are detailed in the Supporting Information.

Surface-Solvent Ion Exchange Thermodynamics

While DFT energies are sufficient to reliably predict aqueous reaction energies, the treatment of solvation in some cases is problematic and can lead to errors. Instead of employing DFT solvation models, here we adopt the Hess' law approach of Rong and Kolpak.[91] We perform DFT calculations to compute the adsorption energies of Li and water products on oxide terminated surfaces, labeled ΔG_1. We supplement DFT calculable surface-slab energies with tabulated experimental values of electrochemical potentials relative to the Standard Hydrogen Electrode (SHE). These experimental ΔG^0_{SHE} values can predict whether an oxide surface of variable coverage with adsorbed species A is stable, or if dissolution is thermodynamically preferred at a given set of conditions. We can incorporate the experimental electrochemical potentials relative to the SHE with the given set of reaction conditions. This equation is labeled ΔG_2, where:

$$\Delta G_2 = \Delta G^0_{\mathrm{SHE}} - n_e(eU_{\mathrm{SHE}}) - 2.303 n_{\mathrm{H}^+} kT\mathrm{pH} + kT\ln a_{\mathrm{H}_x\mathrm{AO}_y^{z-}} \quad (9)$$

We follow the procedure of Rong and Kolpak[91] to obtain calculable Pourbaix diagrams that include the solvation free energies of each species A for the relevant electrochemical equilibria of species A in aqueous solution. We focus on varying compositions of Li and H-terminated surfaces whose main species at experimental reaction conditions are:

$$\mathrm{Li}(s) \leftrightarrow \mathrm{Li}^+(aq) + e^- \quad (10)$$

$$\frac{1}{2}\mathrm{H}_2(g) \leftrightarrow \mathrm{H}^+(aq) + e^- \quad (11)$$

We compute an overall change in free energy, ΔG, that is a combination of DFT calculated adsorbate surface slab free energies (ΔG_1) and experimental dissolution free energies (ΔG_2).

$$\Delta G = \Delta G_1 + \Delta G_2 \tag{12}$$

Results and Discussion

Bulk and Surface Structures

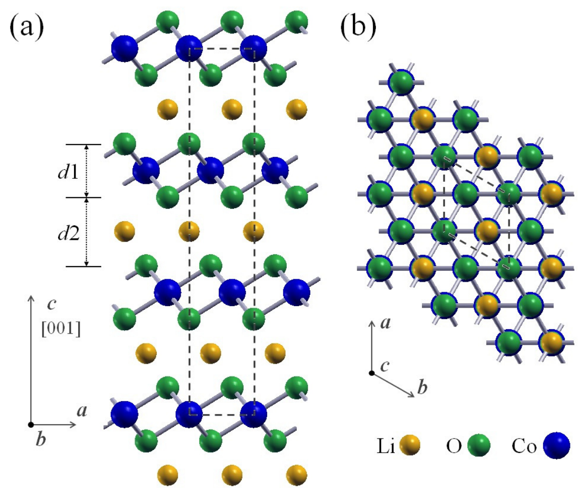

Figure 1: a) Side and b) top views of bulk hexagonal $LiCoO_2$. Each Co^{3+} (blue atom) is octahedrally coordinated to six O^{2-} (green atoms), and each octahedron is corner-sharing with its neighbors. Intercalated between each CoO_2^{-1} layer is a Li^{1+} cation (yellow atom). In a) $d1$ is the vertical intraplanar distance of the octahedra (-O-Co-O-), and $d2$ is the vertical interplanar distance between the octahedra (-O-Li-O-).

Figure 1 shows the a) side and b) top views of bulk hexagonal $LiCoO_2$ of crystal structure $R\bar{3}m$ (space group #166) symmetry . Each Co^{3+} (blue atoms) is octahedrally coordinated to six O (green atoms), and each octahedron is corner-sharing with its neighbors. Intercalated between each CoO_2 layer is a Li^{1+} cation (yellow atoms). Packed along the [001] surface normal, we highlight two distances in Figure 1a; $d1$ is the vertical intraplanar distance of the octahedra, and $d2$ is the vertical interplanar distance between the octahedra. Octahedrally bound Co^{3+} has a low spin $3d^6$ electronic state, and therefore no unpaired electrons.[92]

As DFT underestimates the band gap of transition metal oxides, we apply a Hubbard

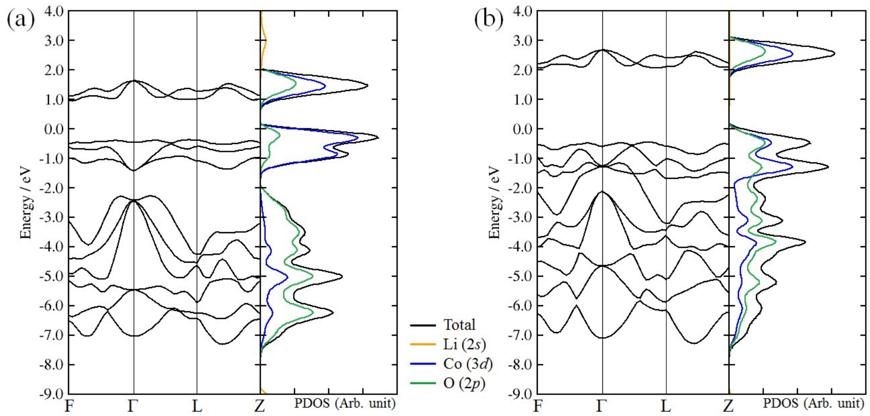

Figure 2: Electronic band structure and corresponding projected density of state (PDOS) of bulk $LiCoO_2$ a) without Hubbard U on Co and b) with Hubbard U=4.91 eV on Co. Addition of U increases the band gap of bulk $LiCoO_2$ from 1.4 to 2.5 eV, close to the experimentally determined[44] and hybrid-functional computed value[50] of 2.7 eV

U correction to the Co. Displayed in Figure 2 is the band structure of hexagonal $LiCoO_2$ a) before U, and b) with U=4.91 eV. This has the effect of opening up the band gap from 1.4 eV to 2.5 eV, closer to the value of 2.7 eV as determined in Refs[44,50] These values are also reported in Table 1. We find similar trends to the change in electronic band structure with the addition of U as those presented in Ref.[50] The bands in the energy interval of -5.0 to -2.0 eV in Figure 2a) are adjusted closer to the Fermi level in b), interacting more with the highest occupied molecular orbitals (HOMO), as the the lowest unoccupied molecular orbitals (LUMO) are shifted from 1.0 (a) to 2.0 eV (b).

Table 1: The comparison of experimental and calculated cell parameters and band gap using different methods for bulk $LiCoO_2$. Percentage errors are shown in parentheses. The $d1$ and $d2$ indicate the interlayer distance shown in Figure 1.

	Expt.	DFT	DFT + U
Wyckoff positions u	0.260	0.261	0.260
$a = b$ / Å	2.814	2.850 (+1.27 %)	2.840 (+0.90 %)
c / Å	14.05	13.90 (-1.09 %)	13.97 (-0.55 %)
$d1$ (O-Co-O) / Å	2.049	2.005 (-2.13 %)	2.032 (-0.81 %)
$d2$ (O-Li-O) / Å	2.634	2.627 (-0.28 %)	2.625 (-0.34 %)
Co–O bond length / Å	1.922	1.927	1.929
Band gap / eV	2.7	1.4	2.5

Calculated bulk parameters of $LiCoO_2$ are presented in Table 1. DFT calculations at the GGA level yield a=2.850 Å and c=13.90 Å, where the lattice constant a is overestimated by 1.27%, and c is underestimated by 1.09%. GGA + U calculations yield a=2.840 Å and c=13.97 Å, where the lattice constant a is only overestimated by 0.90%, and the c increases to 0.07 Å, more in line with experimental data. The adjustment in lattice constant also affects the intra- and interlayer spacings $d1$ (-O-Co-O-) and $d2$ (-O-Li-O-) shown in Figure 1. Addition of U to Co moderately increases $d1$ from 2.005 to 2.032 Å much closer to the experimentally determined value of 2.049 Å and slightly decreases $d2$ from 2.627 to 2.625 Å, which was already very close to the experimentally determined value of 2.634 Å. The net effect is a better description of $d1$ with minimal perturbation to $d2$.

Kramer *et al.*[34] computationally determined that $LiCoO_2$ nanoparticles had at least three thermodynamically stable surfaces, and of this these we choose the polar (001) surface for study for two reasons. Experimental synthesis of nanoscale LCO shows formation of nanoflakes with large (001) planes[22] and the (001) surface was determined to be present for all reasonable values of chemical potential for Li and O,[34] referred to as μ_{Li} and μ_O, respectively. Two common (001) LCO surface terminations, a) oxide-terminated, and b) lithium-terminated are shown in Figure 3. All of the simulated surface slabs have inversion symmetry with at least 11 atomic layers. The slabs are separated by > 16 Å of vacuum space.

Away from vacuum conditions, many oxide surfaces persist with non-stoichiometric configurations, and are terminated with water dissociation products. To explore the thermodynamically preferred hydrated surface structures under ambient conditions, we model Li, Li/OH, and OH terminated surfaces 100%, 75%, 50%, and 25% coverage. To systematically investigate these surface structures, we adopt the following methodology: in –CoO-Li_x surfaces, the outermost Li atoms occupy the crystallographic hollow sites that are the continuation of the bulk arrangement, while in the –CoO-H_x case the adsorbed H atoms are found to be directly above the surface O sites. Thus the terminal H and Li atoms are crystallographically distinct. There is only one atomic site in each layer in the 1×1 supercell, which

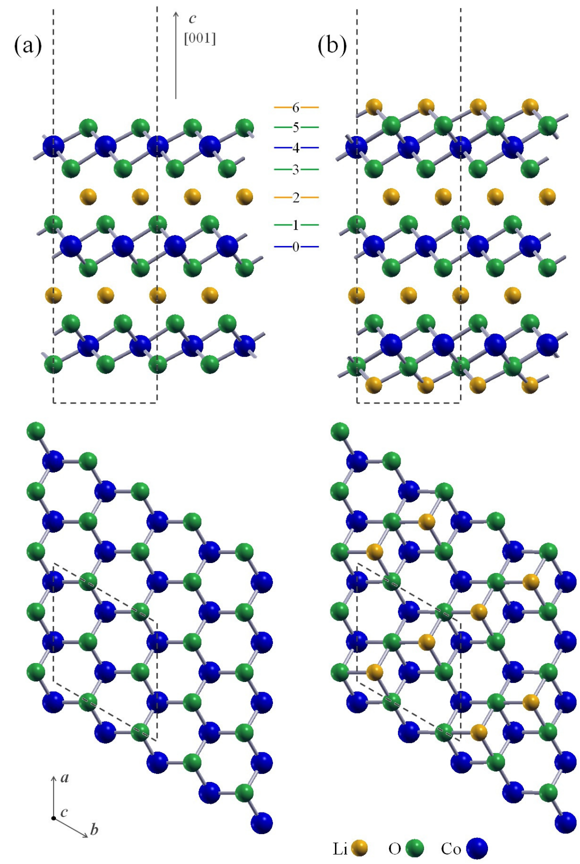

Figure 3: (001) Surface terminations of $LiCoO_2$. Shown in a) is the oxide terminated surface, and shown in b) is the Li-terminated surface. Atomic layers are labeled such that the center of inversion is the (blue) cobalt layer labeled 0 and all odd-numbered layers will be oxygen (green atom) and all even-numbered layers will be either lithium (gold atom) or cobalt.

when occupied corresponds to 100 % coverage. Layers of lower coverages were simulated using (2×2) supercells to obtain coverages down to 25%. Figure 4 shows example surfaces that are a) Li-terminated, b) mixed Li and H terminated, and c) H-terminated.

Surface Thermodynamics

Figure 5 shows the GGA + U-computed 1-Dimensional thermodynamic phase diagrams of four fixed values of $\mu_{\mathrm{rel,Li}}$. As the $\mu_{\mathrm{rel,Li}}$ value decreases from left to right in Figures 5(a) to (d), the range of available $\mu_{\mathrm{rel,O}}$ decreases. This is because of the chemical potential equilibrium condition $\mu_{\mathrm{LiCoO_2}} = \mu_{\mathrm{Li}} + \mu_{\mathrm{Co}} + 2\mu_{\mathrm{O}}$. This also means that for the sets of structures with $N_{\mathrm{Co}} > N_{\mathrm{Li}}$, the coefficient of μ_{Li} in Equation 8 is negative; the calculated value of γ

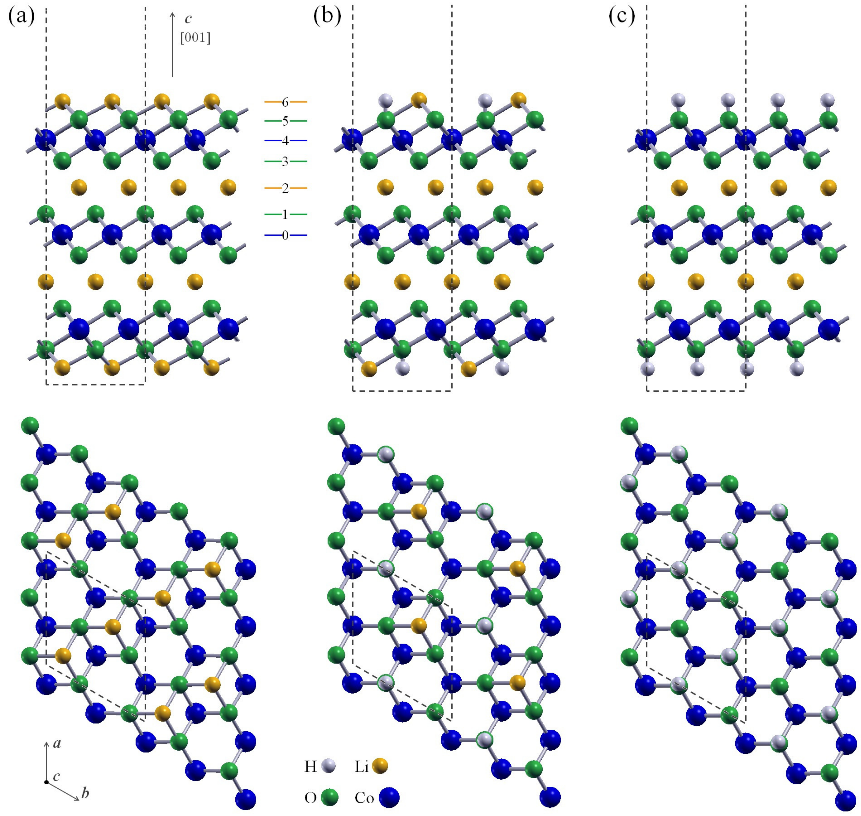

Figure 4: Comparison of select surfaces investigated in the present work showing the side and top views of the (001) surface terminations. Labeling of atomic layers is the same as in Figure 3. From left to right are a) 50% Li-surface coverage b) mixed Li (25%) and H (25%) surface coverage, and c) 50% H-surface coverage. While Li resides in a hollow site that is a continuation of the bulk continuum, H resides directly over alternating surface oxygen to create an -OH surface termination.

increases when μ_{Li} decreases. For the different possible surface terminations, both –CoO and –LiO are O-terminated surfaces, however the latter has much higher surface free energy in Figure 5, as breaking the Co–O bonds in octahedral CoO_6 is energetically unfavorable when compared to breaking the Li-O bonds in the same environment. Due to the same reason, the stoichiometric –CoO-$Li_{1/2}$ and –LiO-$Co_{1/2}$ surfaces have γ values that are independent of μ_{Li} values, and therefore the latter is higher in surface free energy, purely from considering bond strengths alone. Therefore our hydroxylated and Li-terminated surfaces in different coverages are all based on the –CoO-X-Y terminated surface. The only exception is the O-defect surface of –$CoO_{3/4}$. It is not stoichiometric but still maintains charge balance, is

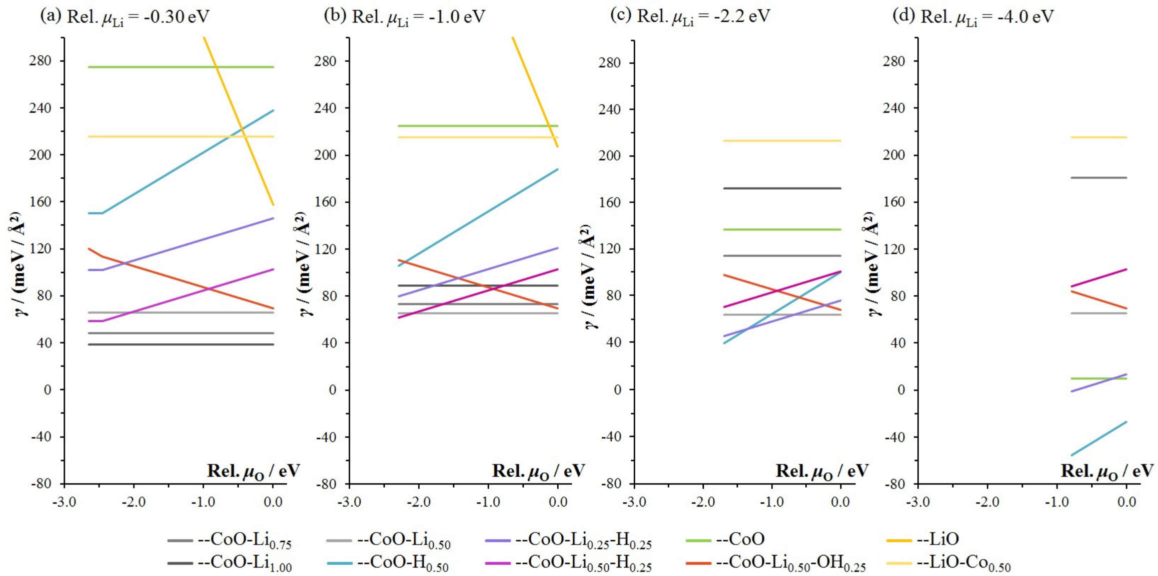

Figure 5: 1-Dimensional thermodynamic phase diagram for four fixed values of $\mu_{\text{rel,Li}}$. As $\mu_{\text{rel,Li}}$ decrease from a) -0.30 eV to d) -4.0 eV, the order of the surfaces lowest in surface free energy γ changes, as does the range of available $\mu_{\text{rel,O}}$. At small, negative values of $\mu_{\text{rel,Li}}$ we are in the Li-rich regime, where the most favored surfaces are -CoO-Li$_x$ terminated (a, gray lines). As $\mu_{\text{rel,Li}}$ decreases, taking us into the Li-poor region, the preferred surface coverage changes until at d) the most favorable surface termination is -CoO-H$_x$, the hydroxylated surface shown in Figure 4(c).

less polar, and lower in free energy than the ideal –CoO surface. Table 2 details the changes in relaxed structure layer spacing for the -CoO, -CoO-Li$_{1/2}$, -CoO-Li$_{1/4}$-H$_{1/4}$ and -CoO-H$_{1/2}$ surfaces when compared to experiment.

In Figure 5(a) when μ_{Li}=-0.30 eV, near the Li-rich limit, the Li-term –CoO-Li$_{3/4}$ surface (dark gray line) is most stable: this surface has the lowest γ for the entire range of μ_{O}. However when μ_{Li} decreases to -1.0 eV in Figure 5(b), a Li-H-mixed surface domain –CoO-Li$_{1/4}$-H$_{1/2}$ begins to appear (magenta line) in the O-poor limit on the left hand-side as the surface lowest in free energy. This occurs for a narrow range of μ_{O}, and is quickly following by a H-terminated surface of –CoO-H$_{3/4}$ (light gray line) which is much lower in free energy for the remainder of μ_{O} through the O-poor limit. When μ_{Li} is decreases further in Figure 5(c) and (d), the –CoO-H$_{3/4}$ surface (light blue line) becomes the only stable surface throughout the entire range of $\mu_{\text{rel,O}}$. This is the surface that one is most likely to encounter at ambient conditions.

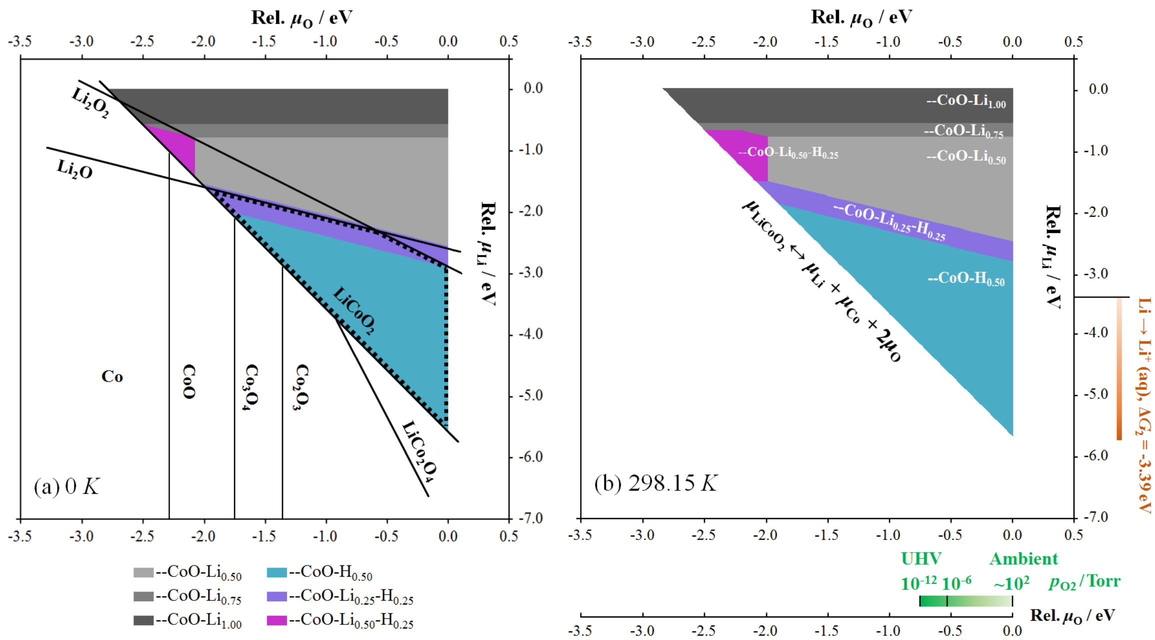

Figure 6: 2-Dimensional surface phase diagram at a) 0 K and b) 298.15 K. Li-terminated surfaces are light, medium, and dark gray, while the pure H-terminated surface in light blue, and the mixed Li/H-terminated surfaces are purple or magenta. In a) we overlay the bulk stability regions of Co, CoO, Co_3O_4, Co_2O_3, Li_2O_2, Li_2O, LiCo2O4, and $LiCoO_2$ to highlight where the computed surface phase diagram overlaps with bulk LCO (dotted black line). We compute minimal changes in the phase diagram in extrapolating from 0 to 298.15 K. Shown on the right-hand side of the figure are the pressure and Li cation equilibrium conditions salient to experiment. The experimentally attainable oxygen rich regime can be found for $\mu_{\text{rel,O}}$ greater than $\approx$ -0.7 eV, as determined by the pressure conversion bar in the bottom right hand corner. Below $\mu_{\text{rel,Li}}$=-3.39 eV, Li will most likely be observed as an aqueous Li^{1+} cation.

Figure 6 shows the 2-dimensional thermodynamic phase diagram at a) O and b) 298.15 K, where the most stable surfaces for different ranges of $\mu_{\text{rel,O}}$ and $\mu_{\text{rel,Li}}$ are color coded. Li-terminated surfaces are light, medium, and dark gray, while the pure H-terminated surface in light blue, and the mixed Li/H-terminated surfaces are purple or magenta. This diagram is shaped like a triangle where the empty boundary represents the thermodynamic limit to maintain bulk E_{LiCoO_2}, based on the equilibrium condition $\mu_{\text{LiCoO}_2} = \mu_{\text{Li}} + \mu_{\text{Co}} + 2\mu_{\text{O}}$. We observe minor changes in Figure 6 extrapolating from T=0 K (a) to T=298.15 K (b); the largest change is observed in the (magenta colored) Li/H co-terminated surface, however this surface is most likely not observable in experiment. On the bottom right hand-side of the figure, we label the pressure conditions on the μ_O axis, and see that the range of ambient to UHV O_2 pressures only change the μ_O by ≈ 0.7 eV.

Starting in the top right hand corner of Figure 6(b), in the O-rich/Li-rich regime we observe the –CoO-Li surface first, and then as we adjust μ_{Li} to lower values at fixed μ_O, we observe the –CoO-$Li_{3/4}$ surface and then the –CoO-$Li_{1/2}$ surface. As we decrease μ_{Li}, we enter Li-poor regimes that are still rich in O. Upon subsequent decreases, we observe the mixed –CoO-$Li_{1/4}$-$H_{1/4}$ surface, and then the –CoO-$H_{1/2}$ surface. This is supported by electrochemical data as well: ΔG^0_{SHE} of Li is -3.039 eV, so decreasing μ_{Li} beyond this point will most likely result in the release of Li^{+1} ions. This regime coincides with a Li-poor/O-rich phase which corresponds to ambient conditions.

Table 2: Comparison of the change in percentage of the layer spacings of optimized $LiCoO_2$ (001) surface structures: –CoO, –CoO-$Li_{0.50}$, –CoO-$Li_{0.25}$-$H_{0.25}$ and –CoO-$H_{0.50}$. The numbers of different atomic layers are labeled in Figure 3 and 4.

	–CoO	–CoO-$Li_{0.50}$	–CoO-$Li_{0.25}$-$H_{0.25}$	–CoO-$H_{0.50}$
O–H bond length / Å			0.974	0.975
Layer 5–6 / %		-32.6	-26.2	
Layer 4–5 / %	-15.0	-0.68	-3.29	-5.04
Layer 3–4 / %	+2.56	-0.60	-0.32	-0.23
Layer 2–3 / %	+1.04	+0.14	+0.11	+2.36
Layer 1–2 / %	-1.15	-0.53	-0.49	-1.85
Layer 0–1 / %	-0.28	-0.46	-0.47	+0.06

The Projected density of states (PDOS) of the surfaces in Figure 6 that occur in the Li-poor/O-rich regime are shown in Figure 7. We find that as H substitutes for Li as μ_{Li} decreases, the band gap also decreases. This decrease occurs as the bonding to surface O changes from Li bound to the hollow O-site, where it interacts with three O, to H bound on top of O. The lowest unoccupied molecular orbital (LUMO) of O decreases in energy relative to the LUMO of Co as the surface changes with a decrease in μ_{Li}.

Figure 8 shows the charge density difference (taken as the charge density of the slab minus the sum of the atomic charge densities), plotted as isosurfaces, for the a)–CoO-$Li_{1/2}$

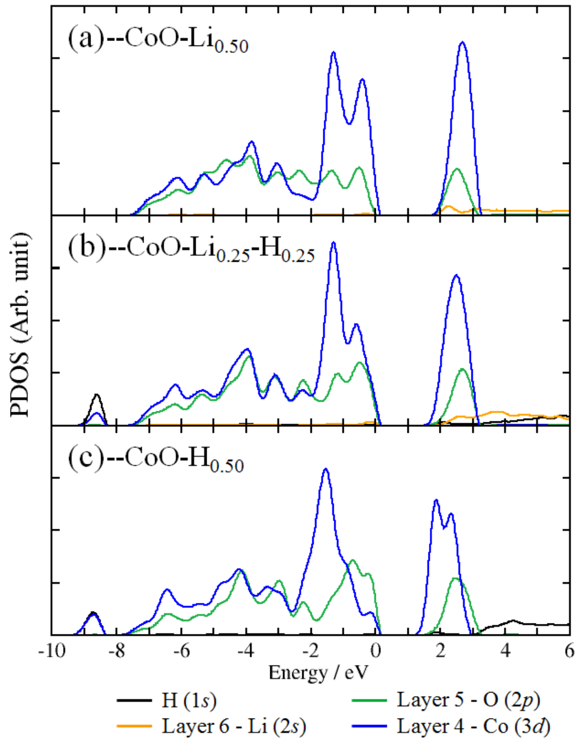

Figure 7: Projected density of states (PDOS) for the three surfaces of Figure 6 that occur in the Li-poor/O-rich regime. These three surfaces are in order of decreasing μ_{Li}: a)–CoO-$Li_{1/2}$ b) –CoO-$Li_{1/4}$-$H_{1/4}$ and c) –CoO-$H_{1/2}$ and show that as H substitutes Li, the band gap decreases.

b) –CoO-$Li_{1/4}$-$H_{1/4}$ and c) –CoO-$H_{1/2}$ terminated surfaces. The turquoise and red colors indicate positive and negative isosurface values, respectively. For the –CoO-$Li_{1/2}$ surface on the left hand side of Figure 8 there is no isosurface expanding out of the slab, and the negatively valued isosurfaces corresponding to surface O sites are localized closely to the surface. The –CoO-$Li_{1/2}$ surface shows relatively neutral charge difference within the surface plane. Substituting half of the Li with H in b) shows a distinct positive isosurface distribution above the H in –CoO-$Li_{1/4}$-$H_{1/4}$ as well as a change in negative isosurface distribution around the surface O relative to the –CoO-$Li_{1/2}$ surface. Full substitution of Li with H, as in c) shows the same distinct positive isosurface distribution above the H in surface OH. We interpret these plots as evidence that there is a depletion of electron density at the OH terminated surfaces relative to the Li terminated surfaces, and this interplay between surface stoichiometry and charge distribution will impact surface reactivity.

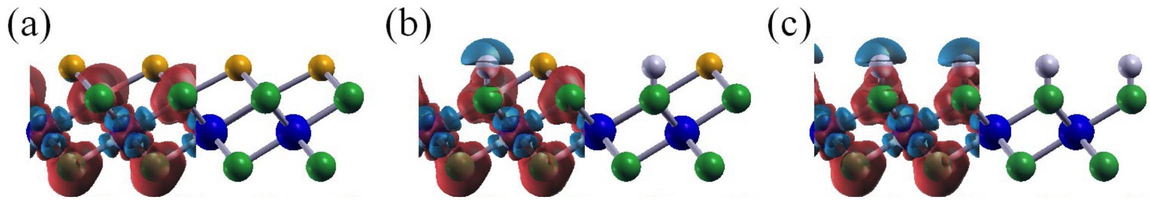

Figure 8: Charge density isosurface difference of a)–CoO-$Li_{1/2}$ b) –CoO-$Li_{1/4}$-$H_{1/4}$ and c) –CoO-$H_{1/2}$ terminated surfaces. The differences in charge density are depicted in turquoise and red colors which indicate positive and negative isosurfaces, respectively. We find that the largest differences between the three occur on the surface as the terminations change from pure Li to mixed Li/H to pure H going from left to right. The space above the (yellow) surface Li atoms displays no positive isosurface, while the space above the (white) surface H atoms displays a positive isosurface. The H-termination creates a dipole relative to the oxygen layer closest to the surface, and will affect (001) surface reactivity.

Next, we turn to computing the thermodynamics of surface solvent ion exchange. As depicted in Figure 9a, conventional DFT simulations predict that all Li surface coverages will be energetically more favorable than any H surface coverages, with the exception of $H_{1/2}$ which is almost degenerate in energy with $Li_{3/4}$ coverage. We find that successive additions of Li from no (x=0) to full (x=1) coverage are energetically more stable with the addition of Li, and that the change in energy between successive increased coverages decreases. This is in contrast to H coverage, where we observe the same behavior until $x=\frac{1}{2}$, where it becomes energetically costly to successively add more H to the surface.

When we add in the surface solvent ion exchange term, ΔG_2, the overall trend switches because it is more energetically favorable to dissolve Li^{1+} from the surface of the oxide than H^+. The ΔG^0_{SHE} terms at pH =7 for Li and H are -3.039 and -0.414 eV, respectively and adjusting the equation:

$$\Delta G_2 = \Delta G^0_{\mathrm{SHE}} - n_e(eU_{\mathrm{SHE}}) - 2.303 n_{\mathrm{H}^+} kT\,\mathrm{pH} + kT \ln a_{\mathrm{H}_x\mathrm{AO}_y^{z-}} \tag{13}$$

with parameters provided by our experimental collaborators: $a_{H_xAO_y^{z-}} = 1\times10^{-6}$, n_{H^+}=0, and U_{SHE}=0 at pH=7, we obtain ΔG_2 of Li to be -3.39 eV and H remains unchanged, as

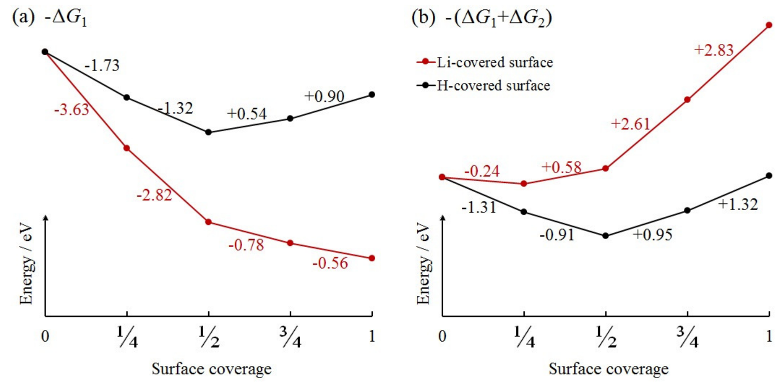

Figure 9: Difference in free energy as a function of surface coverage for a) ΔG_1 and b) using the surface-solvent exchange model (ΔG=ΔG_1+ΔG_2) outlined in Ref.[91] Free energies reported are the difference in free energy between surface coverages. Adding the experimentally determined ΔG_2 values not only changes the magnitude of the free energies for both Li and H adsorption, but reverses the trend observed for all surface coverages. H-terminations are more energetically favorable than Li-terminations with the inclusion of ΔG_2.

ΔG_2^H = -0.0591pH or -0.414 eV.

We find that only $Li_{1/4}$ surface coverage is slightly favored, and that at these conditions it is energetically unfavored to go beyond this coverage. This is opposite to the trends for H, for which all coverages are favorable, but the overall most favored is $H_{1/2}$ surface coverage. Overall, the results are consistent with the phase diagrams discussed in the previous sections. At these experimental conditions, the Li-poor/O-rich regime, surface hydroxyls shown in Figures 4 and 8(c) will be the most energetically favorable surface species.

To probe the reactivity of the different surface terminations, specifically H vs. Li terminated LCO, we choose $H_2PO_4^-$ as our probe adsorbate. $H_2PO_4^-$ is the predominant molecular species at pH 7 and ambient environmental conditions. We model the adsorbate in both monodentate and bidentate configurations where either one or two of the oxygen atoms of phosphate anion, respectively, are interacting with the -CoO-$Li_{1/2}$ or -CoO-$H_{1/2}$ surfaces. These calculations are performed with implicit solvent, as detailed in the Methodology, and structural information can be found in the Supporting Information. We find that both mono- and bi-dentate configurations of outer-sphere adsorption interactions with the Li-terminated surface are endothermic, and that both adsorption interactions with the H-terminated sur-

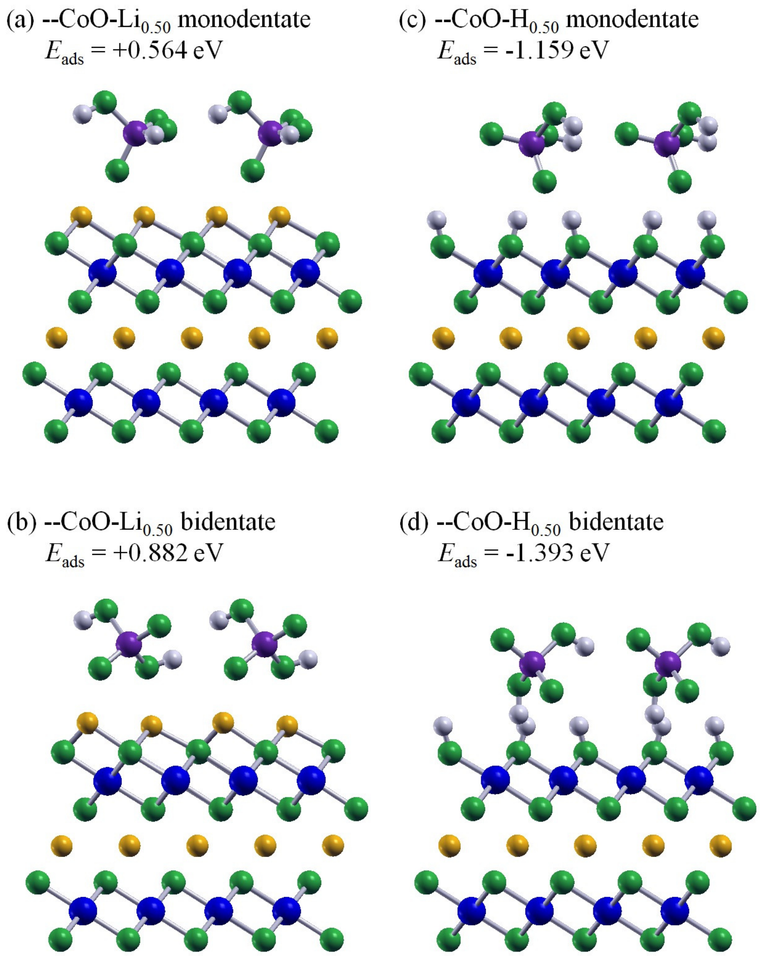

Figure 10: Comparison of mono- and bi-dentate outer sphere adsorption of phosphate with either Li- or H-terminated surfaces. $H_2PO_4^-$ interactions with -CoO-$Li_{1/2}$ are endothermic and interactions with -CoO-$H_{1/2}$ are exothermic. This may be due to hydrogen bonding between the phosphate ligand and OH groups on the surface of c) and d) that are not present in a) and b)

face are exothermic, as depicted in Figure 10. A comparison of the adsorption energies E_{ads} of interaction modes show opposing trends; the changes in energy going from mono- to bi-dentate adsorption are +0.324 eV and -0.234 eV for the Li and H terminated surfaces, respectively. These trends in E_{ads} are consistent with the charge density differences calculated for the surfaces and shown in Figure 8. That is, the OH terminated surfaces showing depleted electron density in the isosurface analysis go on to be the most reactive towards the negatively charged phosphate.

Figure 11 compares the induced charge density of outer sphere monodentate phosphate adsorption on a) the -CoO-$Li_{1/2}$ and b) -CoO-$H_{1/2}$ terminated surfaces. The Li-terminated surface does not interact as much as the H-terminated surface, which displays a sizable hydrogen bonding between the surface and phosphate, and is most likely stabilizing the interaction. This type of bonding network could help explain why phosphate based coating of LCO nanoparticles are favorable in the industrial production of battery materials, bind irreversibly to metal oxides as an environmentally acquired coating, and could have far reaching implications on the design and reactivity of nanomaterials.

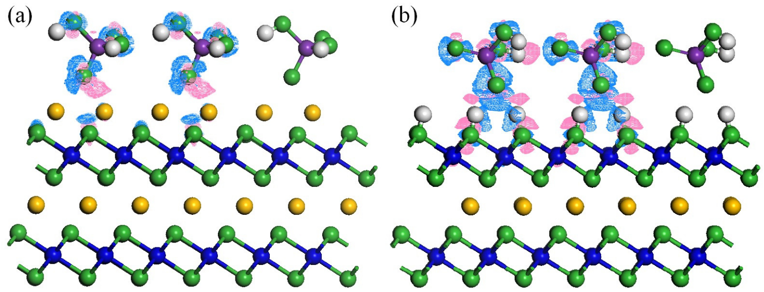

Figure 11: Induced charge density profiles of outer sphere monodentate phosphate adsorption on a) -CoO-$Li_{1/2}$ and b) -CoO-$H_{1/2}$ terminated surfaces. Pink and blue colors indicate an increase and decrease in electron density relative to the bare surfaces, respectively. The -CoO-$H_{1/2}$ terminated surface clearly interacts with phosphate more than the -CoO-$Li_{1/2}$ terminated surface.

Conclusions

$LiCoO_2$ nanoparticles have witnessed a rapid growth in use as battery materials, however, not much has been published on the surface reactivity of LCO in a variety of experimentally accessible scenarios. The need to relate theoretical calculations to real-world conditions is necessary in the pursuit of delineating structure-property relationships of nanomaterials in environmental and operational settings. As structure is linked to reactivity, a molecular-level understanding of how surface stoichiometry and electronic structure evolves as a function of conditions is crucial to identifying surface-mediated processes that govern the toxicity of nanomaterials. This study applies two thermodynamic models in conjunction with DFT calculations to assess the stability of varying $LiCoO_2(001)$ terminations in the presence of oxygen and water. We find that for both models, the -CoO-$H_{1/2}$ surface is the most stable structure near the O-rich limit, which is most likely to be encountered experimentally. A key result of the study is that while both partial OH and partial Li terminations are stable under different chemical potential conditions, the like-charge H and Li cations occupy unique surface sites. Furthermore, exchange of surface Li for H (as predicted to be stable under ambient conditions by our models) leads to distinct surface electronic structure at the surface. This manifests as a marked change in surface reactivity, as we probe through outer-sphere phosphate adsorption studies. We find that outer-sphere adsorption on the Li-terminated surface is energetically unfavored when compared to the H-terminated surface, in line with the depletion of electronic charge on the latter. The theoretical studies performed here demonstrate the sensitivity of the surface structure to changes in the chemical environment. These changes in surface stoichiometry are then shown to alter the electronic structure, and ultimately give rise to unique surface reactivity. Understanding differences in reactivity of these surfaces could have a significant impact on the design of battery materials and may help to explain why coatings bind strongly, and in some cases, irreversibly, to LCO and related nanomaterials.

Associated Content

The Supporting Information is available free of charge on the ACS Publications website at DOI:xxxx

Presented in the Supporting Information are structural details of relaxed surfaces, methodology details, simulation parameters and adsorption geometries.

Author Information

Corresponding Author: sara-mason@uiowa.edu

Notes: The authors declare no competing financial interest.

Acknowledgments

This work was supported by National Science Foundation Center for Chemical Innovation Program grant CHE-1503408 for the Center for Sustainable Nanotechnology. This research was supported in part through computational resources provided by The University of Iowa, Iowa City, Iowa. This work used the Extreme Science and Engineering Discovery Environment (XSEDE[93]), which is supported by National Science Foundation grant number ACI-1053575. X.H., J.W.B., and S.E.M. thank Profs. Qiang Cui and Rigoberto Hernandez for useful discussions of this work.

References

(1) Sapsford, K. E.; Algar, W. R.; Berti, L.; Gemmill, K. B.; Casey, B. J.; Oh, E.; Stewart, M. H.; Medintz, I. L. Functionalizing Nanoparticles with Biological Molecules: Developing Chemistries that Facilitate Nanotechnology. *Chem. Rev.* **2013**, *113*, 1904–2074.

(2) Cui, Q.; Hernandez, R.; Mason, S. E.; Frauenheim, T.; Pedersen, J. A.; Geiger, F. Sustainable Nanotechnology: Opportunities and Challenges for Theoretical/Computational Studies. *J. Phys. Chem. B* **2016**, *120*, 7297–7306.

(3) Lim, S. Y.; Shen, W.; Gao, Z. Carbon Quantum Dots and Their Applications. *Chem. Soc. Rev.* **2015**, *44*, 362–381.

(4) Dunn, J. B.; Gaines, L.; Kelly, J. C.; James, C.; Gallagher, K. G. The Significance of Li-Ion Batteries in Electric Vehicle Life-Cycle Energy and Emissions and Recycling's Role in its Reduction. *Energy Environ. Sci.* **2015**, *8*, 158–168.

(5) Murphy, C. J.; Vartanian, A. M.; Geiger, F. M.; Hamers, R. J.; Pedersen, J.; Cui, Q.; Haynes, C. L.; Carlson, E. E.; Hernandez, R.; Klaper, R. D.; Orr, G.; Rosenzweig, Z. Biological Responses to Engineered Nanomaterials: Needs for the Next Decade. *ACS Cent. Sci.* **2015**, *1*, 117–123.

(6) Alkaliany, A. M.; Murphy, C. J. Toxicity and Cellular Uptake of Gold Nanoparticles: What Have We Learned so Far? *J. Nanoparticle Res* **2010**, *12*, 2313–2333.

(7) Dreaden, E. C.; Alkalany, A. M.; Huang, X.; Murphy, C. J.; El-Sayed, M. A. The Golden Age: Gold Nanoparticles for Biomedicine. *Chem. Soc. Rev.* **2012**, *41*, 2740–2779.

(8) Liu, N.; Hu, L.; McDowell, M. T.; Jackson, A.; Cui, Y. Prelithiated Silicon Nanowires as an Anode for Lithium Ion Batteries. *ACS Nano* **2011**, *5*, 6487–6493.

(9) Park, M.-H.; Kim, M. G.; Joo, J.; Kim, K.; Kim, J.; Ahn, S.; Cui, Y.; Cho, J. Silicon Nanotube Battery Anodes. *Nano Lett.* **2009**, *9*, 3844–3847.

(10) Ko, M.; Chae, S.; Ma, J.; Kim, N.; Lee, H.-W.; Cui, Y.; Cho, J. Scalable Synthesis of Silicon-Nanolayer-Embedded Graphite for High-Energy Lithium-Ion Batteries. *Nature Energy* **2016**, *1*, 16113.

(11) Herle, P. S.; Ellis, B.; Coombs, N.; Nazar, L. F. Nano-Network Electronic Conduction in Iron and Nickel Olivine Phosphates. *Nature Mater.* **2004**, *3*, 147–152.

(12) Yamasaka, S.; Nakamura, Y.; Ueda, T.; Takeuchi, S.; Yamamoto, Y.; Arai, S.; Tanji, T.; Tanaka, N.; Sakai, A. Fabrication of Si Thermoelectric Nanomaterials Containing Ultrasmall Epitaxial Ge Nanodots with an Ultrahigh Density. *J. Electronic Mater.* **2015**, *44*, 2015–2020.

(13) Buchman, J. T.; Gallagher, M. J.; Yang, C.-T.; Zhang, X.; Krause, M. O. P.; Hernandez, R.; Orr, G. Research Highlights: Examining the Effect of Shape on Nanoparticle Interactions with Organisms. *Environ. Sci.: Nano.* **2016**, *3*, 696–700.

(14) Maurer-Jones, M. A.; Gunsolus, I. L.; Murphy, C. J.; Haynes, C. L. Toxicity of Engineered Nanoparticles in the Environment. *Anal. Chem.* **2013**, *85*, 3036–3049.

(15) Lopez-Serrano, A.; Olivas, R. M.; Landaluze, J. S.; Camara, C. Nanoparticles: A Global Vision. Characterization, Separation, and Auantification Methods. Potential Environmental and Health Impact. *Anal. Chem.* **2014**, *6*, 38–56.

(16) Qiu, T. A.; Gallagher, M. J.; Hudson-Smith, N. V.; Wu, J.; Krause, M. O. P.; Fortner, J. D.; Haynes, C. L. Research Highlights: Unveiling the Mechanisms Underlying Nanoparticle-Induced ROS Generation and Oxidative Stress. *Environ. Sci.: Nano* **2016**, *3*, 940–945.

(17) Dominiguez, G. A.; Lohse, S. E.; Torelli, M. D.; Murphy, C. J.; Hamers, R. J.; Orr, G.; Klaper, R. D. Effects of Charge and Surface Ligand Properties of Nanoparticles on Oxidative Stress and Gene Expression Within the Gut of Daphnia magna. *Aquatic Toxicology* **2015**, *162*, 1–9.

(18) Lehman, S. E.; Mudunkotuwa, I. A.; Grassian, V. H.; Larsen, S. C. Nano-Bio Interactions of Porous and Nonporous Silica Nanoparticles of Varied Surface Chemistry: A Structural, Kinetic, and Thermodynamic Study of Protein Adsorption from RPMI Culture Medium. *Langmuir* **2016**, *32*, 731–742.

(19) Qiu, T. A.; Meyer, B. M.; Christenson, K. G.; Klaper, R. D.; Haynes, C. L. A Mechanistic Study of TiO_2 Nanoparticle Toxicity on Shewanella Oneidensis MR-1 with UV-Containing Simulated Solar Irradiation: Bacterial Growth, Riboflavin Secretion, and Gene Expression. *Chemosphere* **2016**,

(20) Troiano, J. M.; Kuech, T. R.; Vartanian, A. M.; Torelli, M. D.; Sen, A.; Jacob, L. M.; Hamers, R. J.; Murphy, C. J.; Pedersen, J. A.; Geiger, F. M. On Electronic and Charge Interference in Second Harmonic Generation Responses from Gold Metal Nanoparticles at Supported Lipid Bilayers. *J. Phys. Chem. C* **2016**, *120*, 20659–20667.

(21) Melby, E. S.; Mensch, A. C.; Lohse, S. E.; Hu, D.; Orr, G.; Murphy, C. J.; Hamers, R. J.; Pedersen, J. A. Formation of Supported Lipid Bilayers Containing Phase-Segregated Domains and Their Interaction with Gold Nanoparticles. *Environ. Sci.: Nano* **2016**, *3*, 45–55.

(22) Dogangun, M.; Hang, M. N.; Troiano, J. M.; McGeachy, A. C.; Melby, E. S.; Pedersen, J. A.; Hamers, R. J.; Geiger, F. M. Alteration of Membrane Compositional Asymmetry by $LiCoO_2$ Nanosheets. *ACS Nano* **2015**, *9*, 8755–8765.

(23) Hang, M. N.; Gunsolus, I. L.; Wayland, H.; Melby, E. S.; Mensch, A. C.; Hurley, K. R.; Pedersen, J. A.; Haynes, C. L.; Hamers, R. J. Impact of Nanoscale Lithium Nickel Manganese Cobalt Oxide (NMC) on the Bacterium Shewanella oneidensis MR-1. *Chem. Mater.* **2016**, 1092–1100.

(24) Notter, D. A.; Gauch, M.; Widmer, R.; Wager, P.; Stamp, A.; Zah, R.; Althaus, H. J. Contribution of Li-ion Batteries to the Environmental Impact of Electric Vehicles. *Environ. Sci. Technol.* **2010**, *44*, 6550–6556.

(25) Choi, N. S.; Chen, Z.; Freunberger, S. A.; Ji, X.; Sun, Y. K.; Amine, K.; Yushin, G.; Nazar, L. F.; Cho, J.; Bruce, P. G. Challenges Facing Lithium Batteries and ELectrical Double Layer Capacitors. *Angew. Chem. Int. Ed.* **2012**, *51*, 9994–10024.

(26) Whittingham, M. S. Lithium Batteries and Cathode Materials. *Chem. Rev.* **2004**, *104*, 4271–4301.

(27) Armand, M.; Tarascon, J. M. Building Better Batteries. *Nature* **2008**, *451*, 652–657.

(28) Johnson, C. S.; Li, N.; Lefief, C.; Vaughey, J. T.; Thackeray, M. M. Synthesis, Characterization and Electrochemistry of Lithium Battery Electrodes: xLi$_2$MnO$_3$-(1-x)LiMn$_{0.333}$Ni$_{0.333}$Co$_{0.333}$O$_2$ where $(0 <= x <= 0.7)$. *Chem. Mater.* **2008**, *20*, 6095–6106.

(29) Belharouak, I.; Sun, Y. K.; Liu, J.; Amine, K. Li(Ni$_{1/3}$Co$_{1/3}$Mn$_{1/3}$)O$_2$ as a Suitable Cathode for High Power Applications. *J. Power Sources* **2003**, *123*, 247–252.

(30) Conry, T. E.; Mehta, A.; Cabana, J.; Doeff, M. M. Structural Underpinnings of the Enhanced Cycling Stability upon Al-Substitution in LiNi$_{0.45}$Mn$_{0.45}$Co$_{0.1-y}$Al$_y$O$_2$ Positive Electrode Materials for Li-ion Batteries. *Chem. Mater.* **2012**, *24*, 3307–3317.

(31) Goodenough, J. B.; Kim, Y. Challenges for Rechargeable Li Batteries. *Chem. Mater.* **22**, *2010*, 587–603.

(32) Poizot, P.; Laruelle, S.; Grugeon, S.; Dupont, L.; Tarascon, J. M. Nano-Sized Transition-Metal Oxides as Negative-Electrode Materials for Lithium-Ion Batteries. *Nature* **2000**, *407*, 496–499.

(33) Zhou, F.; Cococcioni, M.; Marianetti, C. A.; Morgan, D.; Ceder, G. First-Principles Prediction of Redox Potentials in Transition-Metal Compounds with LDA+U. *Phys. Rev. B* **2004**, *70*, 235121–1–8.

(34) Kramer, D.; Ceder, G. Tailoring the Morphology of LiCoO$_2$: A First Principles Study. *Chem. Mater.* **2009**, *21*, 3799–3809.

(35) Islam, M. S.; Fischer, C. A. J. Lithium and Sodium Battery Cathode Materials: Computational Insights into Voltage, Diffusion and Nanostructural Properties. *Chem. Soc. Rev.* **2014**, *43*, 185–204.

(36) Kang, K.; Meng, Y. S.; Breger, J.; Grey, C. P.; Ceder, G. Electrodes with High Power and High Capacity for Rechargeable Lithium Batteries. *Science* **2006**, *311*, 977–980.

(37) Ceder, G.; Chiang, Y.-M.; Sadoway, D. R.; Aydinol, M. K.; Jang, Y.-I.; Huang, B. Identification of Cathode Materials for Lithium Batteries Guided by First-Principles Calculations. *Nature* **1998**, *392*, 694–696.

(38) Hwang, B. J.; Tsai, Y. W.; Carlier, D.; Ceder, G. A Combined Computational/Experimental Study on $LiNi_{1/3}Co_{1/3}Mn_{1/3}O_2$. *Chem. Mater.* **2003**, *15*, 3676–3682.

(39) Morgan, D.; der Ven, A. V.; Ceder, G. Li Conductivity in Li_xMPO_4 (M = Mn, Fe, Co, Ni) Olivine Materials. *Electrochem. Solid State Lett.* **2004**, *7*, A30–A32.

(40) Koyama, Y.; Yabuuchi, N.; Tanaka, I.; Adachi, H.; Ohzuku, T. Solid State Chemistry and Electrochemistry of $LiCo_{1/3}Ni_{1/3}Mn_{1/3}O_2$ for Advanced Lithium-Ion Batteries. *J. ELectrochem. Soc.* **2004**, *151*, A1545–A1551.

(41) Hautier, G.; Jain, A.; Ong, S. P.; Kang, B.; Moore, C.; Doe, R.; Ceder, G. Phosphates as Lithium-Ion Battery Cathodes: An Evaluation Based on High-throughput *ab initio* Calculations. *Chem. Mater.* **2011**, *23*, 3495–3508.

(42) Hautier, G.; Jain, A.; Chen, H.; Moore, C.; Ong, S. P.; Ceder, G. Novel Mixed Polyanions Lithium-Ion Battery Cathode Materials Predicted by High-Throughput *ab initio* Calculations. *J. Mater. Chem.* **2011**, *21*, 17147–17153.

(43) Hu, L.; Xiong, Z.; Ouyang, C.; Shi, S.; Ji, Y.; Lei, M.; Wang, Z.; Li, H.; Huang, X.; Chen, L. *Ab initio* Studies on the Stability and Electronic Structure of $LiCoO_2$ (003) Surfaces. *Phys. Rev. B* **2005**, *71*, 125433–1–10.

(44) van Elp, J.; Wieland, J. L.; Eskes, H.; Kuiper, P.; Sawatzky, G. A. Electronic Structure of CoO, Li-doped CoO, and $LiCoO_2$. *Phys. Rev. B* **1991**, *44*, 6090–6103.

(45) Carlier, D.; derVen, A. V.; Delmas, C.; Ceder, G. First-Principles Investigation of Phase Stability in the O_2-$LiCoO_2$ System. *Chem. Mater.* **2003**, *15*, 2651–2660.

(46) Andriyevsky, B.; Doll, K.; Jacob, T. Electronic and Transport Properties of $LiCoO_2$. *Phys.Chem.Chem.Phys.* **2014**, *16*, 23412–23420.

(47) Aykol, M.; Kim, S.; Wolverton, C. van der Waals Interactions in Layered Lithium Cobalt Oxides. *J. Phys. Chem. C* **2015**, *119*, 19053–19058.

(48) Wang, B.; Li, S. L.; Truhlar, D. G. Modeling the Partial Atomic Charges in Inorganometallic Molecules and Solids and Charge Redistribution in Lithium-Ion Cathodes. *J. Chem. Theory Comput.* **2014**, *10*, 5640–5650.

(49) Xiong, F.; Yan, H. J.; Chen, Y.; Xu, B.; Le, J. X.; Ouyang, C. Y. The Atomic and Electronic Structure Changes Upon Delithiation of $LiCoO_2$ From First Principles Calculations. *Int. J. Electrochem. Sci.* **2012**, *7*, 9390–9400.

(50) Ensling, D.; Thissen, A.; Laubach, S.; Schmidt, P. C.; Jaegermann, W. Electronic Structure of $LiCoO_2$ Thin Films: A Combined Photoemission Spectroscopy and Density Functional Theory Study. *Phys. Rev. B* **2010**, *82*, 195431–1–16.

(51) Moriwake, H.; Kuwabara, A.; Fisher, C. A. J.; Huang, R.; Hitosugi, T.; Ikuhara, Y. H.; Oki, H.; Ikuhara, Y. First-Principles Calculations of Lithium-Ion Migration at a Coherent Grain Boundary in a Cathode Material, $LiCoO_2$. *Adv. Mater.* **2013**, *25*, 618–622.

(52) Moradabadi, A.; Kaghazchi, P. Mechanism of Li Intercalation/Deintercalation into/from the Surface of $LiCoO_2$. *Phys.Chem.Chem.Phys.* **2015**, *17*, 22917–22922.

(53) Ning, F.; Li, S.; Xu, B.; Ouyang, C. Strain Tuned Li Diffusion in $LiCoO_2$ Material for Li Ion Batteries: A First Principles Study. *Solid State Ionics* **2014**, *235*, 46–48.

(54) Shishkin, M.; Sato, H. Self-Consistent Parametrization of DFT + U Framework Using Linear Response Approach: Application to Evaluation of Redox Potentials of Battery Cathodes. *Phys. Rev. B* **2016**, *93*, 085135–1–13.

(55) Haruyama, J.; Sodeyama, K.; Han, L.; Takada, K.; Tateyama, Y. Space-Charge Layer Effect at the Interface between Oxide Cathode and Sulfide Electrolyte in All-Solid-State Lithium-Ion Battery. *Chem. Mater.* **2014**, *26*, 4248–4255.

(56) Xu, B.; Qian, D.; Wang, Z.; Meng, Y. S. Recent Progress in Cathode Materials Research for Advanced Lithium Ion Batteries. *Mater. Sci. Eng. R* **2012**, *73*, 51–65.

(57) Kim, Y.; Veith, G. M.; Nanda, J.; Unocic, R. R.; Chi, M.; Dudney, N. J. High Voltage Stability of $LiCoO_2$ Particles with a Nanoscale Lipon Coating. *Electrochim. Acta.* **2011**, *56*, 6573–6580.

(58) Taminato, S.; Hirayama, M.; Suzuki, K.; Tamura, K.; Minato, T.; Arai, H.; Uchimoto, Y.; Ogumi, Z.; Kanno, R. Lithium Intercalation and Structural Changes at the $LiCoO_2$ Surface under High Voltage Battery Operation. *J. Power Sources* **2016**, *307*, 599–603.

(59) Cho, J.; Lee, J.-G.; Kim, B.; Park, B. Effect of P_2O_5 and $AlPO_4$ Coating on $LiCoO_2$ Cathode Material. *Chem. Mater.* **2003**, *15*, 3190–3193.

(60) Kim, J.; Noh, M.; Cho, J.; Kim, H.; Kim, K.-B. Controlled Nanoparticle Metal Phosphates (M= Al, Fe, Ce, and Sr) Coatings on $LiCoO_2$ Cathode Materials. *J. Electrochem. Soc.* **2005**, *152*, A1142–A1148.

(61) Verdier, S.; Ouatani, L. E.; Dedryvere, R.; Bonhomme, F.; Biensan, P.; Gonbeau, D. XPS Study on Al_2O_3- and $AlPO_4$-Coated $LiCoO_2$ Cathode Material for High-Capacity Li-Ion Batteries. *J. Electrochem. Soc.* **2007**, *154*, A1088–A1099.

(62) Lee, J.-G.; Kim, T.-G.; Park, B. Metal-Phosphate Coating on $LiCoO_2$ Cathodes with High Cutoff Voltages. *Mater. Res. Bull.* **2007**, *42*, 1201–1211.

(63) Lu, Y.-C.; Mansour, A. N.; Yabuuchi, N.; Shao-Horn, Y. Probing the Origin of En-

hanced Stability of $AlPO_4$ Nanoparticle Coated $LiCoO_2$ during Cycling to High Voltages: Combined XRD and XPS Studies. *Chem. Mater.* **2009**, *21*, 4408–4424.

(64) Chen, Z.; Qin, Y.; Amine, K.; Sun, Y.-K. Role of Surface Coating on Cathode Materials for Lithium-Ion Batteries. *J. Mater. Chem.* **2010**, *20*, 7606–7612.

(65) Huang, J.; Luo, J. A Facile and Generic Method to Improve Cathode Materials for Lithium-Ion Batteries via Utilizing Nanoscale Surface Amorphous Films of Self-Regulating Thickness. *Phys. Chem. Chem. Phys.* **2014**, *16*, 7786–7798.

(66) Moses, A. W.; Garcia-Flores, H. G.; Kim, J.-G.; Langell, M. A. Surface Properties of $LiCoO_2$, $LiNiO_2$ and $LiNi_{1-x}Co_xO_2$. *Appl. Surf. Sci.* **2007**, *253*, 4782–4791.

(67) Daheron, L.; Martinez, H.; Dedryvere, R.; Baraille, I.; Menetrier, M.; Denage, C.; Delmas, C.; Gonbeau, D. Surface Properties of $LiCoO_2$ Investigated by XPS Analyses and Theoretical Calculations. *J. Phys. Chem. C* **2009**, *113*, 5843–5852.

(68) Ohzuku, T.; Ueda, A. Solid-State Redox Reactions of $LiCoO_2$ $R\bar{3}m$ for 4 Volt Secondary Lithium Cells. *J. Electrochem. Soc.* **1994**, *141*, 2972–2977.

(69) Kim, Y.; Lee, H.; Kang, S. First-Principles and Experimental Investigation of the Morphology of Layer-Structured $LiNiO_2$ and $LiCoO_2$. *J. Mater. Chem.* **2012**, *22*, 12874–12881.

(70) Maram, P. S.; Costa, G. C. C.; Navrotsky, A. Experimental Confirmation of Low Surface Energy in $LiCoO_2$ and Implications for Lithium Battery Electrodes. *Angew. Chem. Int. Ed.* **2013**, *52*, 12139–12142.

(71) Hohenberg, P.; Kohn, W. Inhomogeneous Electron Gas. *Phys. Rev.* **1964**, *136*, B864–71.

(72) Kohn, W.; Sham, L. J. Self-Consistent Equations Including Exchange and Correlation Effects. *Phys. Rev.* **1965**, *140*, A1133–8.

(73) Perdew, J. P.; Burke, K.; Ernzerhof, M. Generalized Gradient Approximation Made Simple. *Phys. Rev. Lett.* **1996**, *77*, 3865–8.

(74) Giannozzi, P.; Baroni, S.; Bonini, N.; Calandra, M.; Car, R.; Cavazzoni, C.; Ceresoli, D.; Chiarotti, G. L.; Cococcioni, M.; Dabo, I.; et al., Quantum ESPRESSO: A Modular and Open-Source Software Project for Quantum Simulations of Materials. *J. Phys.:Condens. Matter* **2009**, *21*, 395502–20.

(75) Vanderbilt, D. Soft Self-Consistent Pseudopotentials in a Generalized Eigenvalue Formalism. *Phys. Rev. B Rapid Comm.* **1990**, *41*, 7892–5.

(76) Monkhorst, H. J.; Pack, J. D. Special Points for Brillouin-Zone Integrations. *Phys. Rev. B* **1976**, *13*, 5188–5192.

(77) Hubbard, J. Electron Correlation in Narrow Energy Bands. *Proc. R. Soc. Lond. A* **1963**, *276*, 238–257.

(78) Anisimov, V. I.; Zaanen, J.; Anderson, O. K. Bond Theory and Mott Insulators: Hubbard U Instead of Stoner T. *Physical Review B* **1991**, *44*, 943–54.

(79) Anisimov, V. I.; Gunnarsson, O. Density-Functional Calculation of Effective Coulomb Interactions in Metals. *Phys. Rev. B.* **1991**, *43*, 7570.

(80) Anisimov, V. I.; Aryasetiawan, F.; Lichtenstein, A. I. First-principles Calculations of the Electronic Structure of Strongly Correlated Systems: the LDA + U Method. *J. Phys. Cond. Matter* **1997**, *9*, 767.

(81) Cococcioni, M.; de Gironcoli, S. Linear Response Approach to the Calculation of the Effective Interaction Parameters in the LDA + U Method. *Phys. Rev. B* **2005**, *71*, 035105–1–16.

(82) Delley, B. An All-Electron Numerical Method for Solving the Local Density Functional for Polyatomic Molecules. *J. Chem. Phys.* **1990**, *92*, 508–17.

(83) Delley, B. From Molecules to Solids with the DMol^3 Approach. *J. Chem. Phys.* **2000**, *113*, 7756–64.

(84) Klamt, A.; Schuurmann, G. COSMO - A New Approach to Dielectric Screening in Solvents with Explicit Expressions for the Screening Energy and its Gradient. *Journal of the Chemical Society-Perkin Transactions 2* **1993**, *5*, 799–05.

(85) Reuter, K.; Scheffler, M. Composition, Structure, and Stability of RuO_2(110) as a Function of Oxygen Pressure. *Physical Review B* **2001**, *65*, 035406–1–11.

(86) Sun, Q.; Reuter, K.; Scheffler, M. Effect of a Humid Environment on the Surface Structure of RuO_2(110). *Physical Review B* **2003**, *67*, 205424–1–7.

(87) Reuter, K.; Scheffler, M. Composition and Structure of the RuO_2(110) Surface in an O_2 and CO Environment: Implications for the Catalytic Formation of CO_2. *Phys. Rev. B* **2003**, *68*, 045407–1–11.

(88) Wang, X.-G.; Chaka, A.; Scheffler, M. Effect of the Environment on α-Al_2O_3(0001) Surface Structures. *Phys. Rev. Lett.* **2000**, *84*, 3650–3.

(89) Lo, C. S.; Tanwar, K. S.; Chaka, A. M.; Trainor, T. P. Density Functional Theory Study of the Clean and Hydrated Hematite ($1\bar{1}02$) Surfaces. *Phys. Rev. B* **2007**, *75*, 075425–1–15.

(90) Mason, S. E.; Iceman, C. R.; Trainor, T. P.; Chaka, A. M. Density Functional Theory Study of Clean, Hydrated, and Defective Alumina ($1\bar{1}02$) Surfaces. *Physical Review B* **2010**, *81*, 125423–1–16.

(91) Rong, X.; Kolpak, A. M. Ab initio Approach for Prediction of Oxide Surface Structure, Stoichiometry, and Electrocatalytic Activity in Aqueous Solution. *Phys. Chem. Lett.* **2015**, *6*, 1785–1789.

(92) Qian, D.; Hinuma, Y.; Chen, H.; Du, L.-S.; Carroll, K. J.; Ceder, G.; Grey, C. P.; Meng, Y. S. Electronic Spin Transition in Nanosize Stoichiometric Lithium Cobalt Oxide. *J. Am. Chem. Soc.* **2012**, *134*, 6096–6099.

(93) Towns, J.; Cockerill, T.; Dahan, M.; Foster, I.; Gaither, K.; Grimshaw, A.; Hazlewood, V.; Lanthrop, S.; Lifka, D.; Peterson, G. D.; Roskies, R.; Scott, J. R.; Wilkins-Diehr, N. XSEDE:Accelerating Scientific Discovery. *Comp. Sci. Engineering* **2014**, *16*, 62–74.

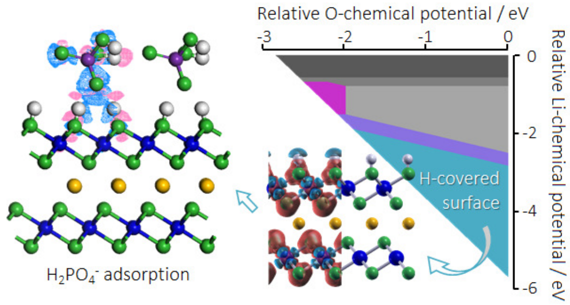

Figure 12: Table of Contents Image